Wireless Links in the Radiative Near Field via Bessel Beams

Jason D. Heebl, Mauro Ettorre, and Anthony Grbic

Phys. Rev. Applied **6**, 034018 — Published 29 September 2016

DOI: 10.1103/PhysRevApplied.6.034018

Wireless Links in the Radiative Near field with Bessel Beams

Jason D. Heebl,[1, *] Mauro Ettorre,[2, †] and Anthony Grbic[1, ‡]

[1] *Radiation Laboratory, Department of Electrical Engineering and Computer Science, University of Michigan, Ann Arbor, MI 48109-2122 USA.*

[2] *Institute d'Electronique et de Télécommunications de Rennes (IETR), UMR CNRS 6164, Université de Rennes 1, Rennes, France.*

(Dated: August 25, 2016)

The generation of propagating Bessel beams is typically limited to optical frequencies with bulky experimental setups. Recent works have demonstrated Bessel beam generation at microwave and millimeter-wave frequencies utilizing low-profile, planar, leaky-wave antennae. These studies have assumed a single leaky mode in the antenna. In this work, the rigorous analysis of a planar Bessel beam launcher supporting multiple modes is presented. By employing the mode-matching technique, a complete electromagnetic solution of the structure, its supported modes, and radiated fields is obtained. Additionally, a coupled system of two planar Bessel launchers is analyzed, and it is shown that the system can both transmit and receive Bessel beams. The energy transfer characteristics of the coupled system are analyzed, and the system's power transfer capabilities discussed. An analysis of the coupled system's even and odd modes of operation show that efficient power transfer is possible, and that an odd mode is preferred, since it yields higher field confinement and power transfer efficiency.

I. INTRODUCTION

Ideal Bessel beams are field solutions to Maxwell's equations which do not undergo diffractive spreading [1]. A Bessel beam can be considered as the superposition of plane waves with propagation constants lying on a cone. They have self-healing capabilities, which allow the field to re-form behind scatterers, and can be tailored to have narrow beam-widths. These extraordinary traits suggest valuable application in the field of near-field probing, medical imaging, and wireless power transfer. However, these idealized beams possessing an infinite non-diffracting range require infinite energy. In addition, practical Bessel beam demonstrations have generally been at optical frequencies [2, 3]. Attempts typically employ an illuminated axicon, or similar lens, to generate Bessel beams over a finite range [4, 5].

In recent literature [6, 7], efforts to realize Bessel beam launchers in the microwave regime have been reported. The leaky radial-waveguide, proposed in [6] as a launcher, is planar, low profile, and fed directly with a coaxial cable. An approximate analysis of the microwave Bessel beam launcher was performed which considered a single leaky mode within the radial waveguide (launcher) [6]. The transverse resonance technique was used to derive the dispersion relation and establish design parameters. The reported structure demonstrated Bessel beam generation within a non-diffractive range above the leaky radial waveguide [7]. The analysis, however, did not consider the presence of other modes, nor were the fields in free-space above exactly solved. A more thorough field solution of the launcher, identifying its modal structure, lies in the mode-matching technique. Mode-matching was first proposed as a solution to waveguide discontinuity problems [8, 9], and has been employed in more recent literature [10–12]. In other recent works, free-space fields are found using mode-matching techniques by applying the Hankel transform [13].

In this paper, a mode-matching approach is applied to the planar Bessel beam launcher (see Fig. 1). The relevant vector potential is defined, and an Eigenmode expansion is employed to express the field solution as a summation of transverse modes. Since the free-space spectrum above the launcher is continuous, it is expressed in terms of the Hankel transform. Power orthogonality relations are employed to preserve continuity of power flow across the structural boundaries. In this way, the solution of the modal coefficients is obtained. This approach allows the relative magnitude of the waveguide modes to be computed, and provides an explicit solution for the free-space (radiated) spectrum.

Since an isolated launcher is known to generate Bessel beams, the analysis is extended to two coupled launchers. In this arrangement, two launchers are separated by a distance d, and the system's ability to transmit *and receive* Bessel beams is demonstrated. As this system of coupled launchers is comprised of two coupled resonators (launchers), the field response exhibits even and odd modes of operation about its central plane. The polarity of the modal coefficients in the launchers identifies these even and odd modes of operation. Two-port scattering parameters are retrieved from the analysis of the coupled launchers. Port impedances are then computed for a simultaneous complex-conjugate impedance-match. The performance of the conjugately matched system is subsequently discussed. The even mode is shown to radiate more, whereas the odd mode demonstrates high field confinement in free-space and the fields between the two Bessel launchers appear as within a waveguide. In

* E-mail:jheebl@umich.edu
† E-mail:mauro.ettorre@univ-rennes1.fr
‡ E-mail:agrbic@umich.edu

other words, a diffractionless beam exists in free-space. Much work has been reported on wireless links as well as power transfer in the reactive near field and far-field [14–17]. Here, the system operates at distances between these two ranges; within the radiative near-field. Additionally, it is shown that the radiative system is highly coupled, as the input impedance is dependent on the receiving launcher. This is unusual for a radiative system, but is the case for the coupled Bessel launchers.

II. SINGLE BESSEL LAUNCHER

In [6, 7], it was shown that an electrically-thin radial waveguide, covered with a capacitive sheet, can produce a propagating Bessel beam. A cross-sectional image of such a structure excited by a coaxial feed is depicted in Fig. 1. Regions I and II both have a central conductor of radius a, and an outer conductor of radius b and c, respectively. Region I represents the coaxial feed used to excite the structure. Region II can be analyzed as an over-sized coaxial waveguide with a discontinuity at $z = -h$. Region III represents free-space, and the boundary between Region II and III is defined by a sheet impedance, Z_{sheet}, at $z = 0$. The sheet impedance specifies the transverse field ratio, $Z_{sheet} = -E_\rho/H_\phi$, and is capacitive. This allows the radial waveguide to support transverse magnetic with respect to $\hat{z}$ (TM^z) leaky waves. Analysis proceeds in the following sections with the derivation of the fields in a coaxial waveguide.

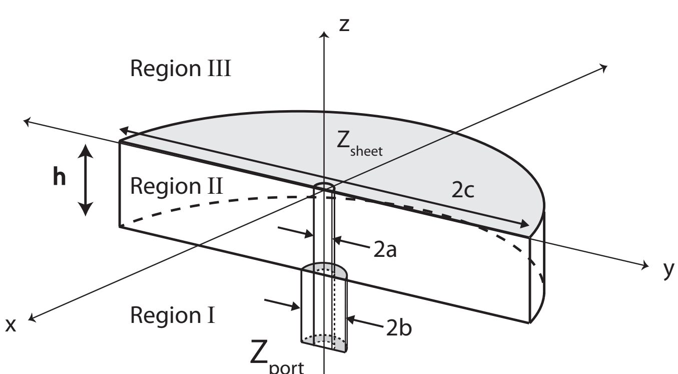

FIG. 1. A cross-sectional view of a leaky radial waveguide capable of launching propagating Bessel beams. All boundaries, excepting Z_{sheet}, are assumed perfect electric conductors (PEC).

A. Review of Field Definitions

Here, expressions for the TM^z modes supported by the coaxial waveguides (Regions I and II) of the Bessel beam launcher are reviewed. The electromagnetic vector potential in either Region I or II can be expressed in separable form [18]:

$$\psi = Z(z)\, R(\rho)\, \Phi(\phi) . \tag{1}$$

The potentials are defined for a coaxial structure with cylindrical geometry. Since the structure and excitation are ϕ-invariant, further expression of $\Phi(\phi)$ is suppressed. The TM^z fields are derived from the vector potential (1) in cylindrical coordinates [18, 19]. The resulting TM^z fields have the form:

$$E_\rho = \frac{1}{\omega\varepsilon} k_\rho k_z \left[A e^{-jk_z z} - B e^{jk_z z}\right] R_1(k_\rho \rho, \rho_1), \tag{2}$$

$$H_\phi = k_\rho \left[A e^{-jk_z z} + B e^{jk_z z}\right] R_1(k_\rho \rho, \rho_1), \tag{3}$$

$$E_z = -\frac{j}{\omega\varepsilon} {k_\rho}^2 \left[A e^{-jk_z z} + B e^{jk_z z}\right] R_0(k_\rho \rho, \rho_1), \tag{4}$$

where $E_\phi = H_\rho = H_z = 0$. A time harmonic progression of $e^{j\omega t}$ is assumed (e^{-jkz} indicates propagation in the $+\hat{z}$ direction). The general form of R is defined as

$$\mathrm{R}_\nu(k_\rho\rho, \rho_1) = \left[J_\nu(k_\rho\rho) - \frac{J_0(k_\rho\rho_1)}{Y_0(k_\rho\rho_1)} Y_\nu(k_\rho\rho)\right], \tag{5}$$

where ρ_1 is the outside-rim of the coaxial conductor, and $J_\nu(k_\rho\rho)$ and $Y_\nu(k_\rho\rho)$ are ν-th order Bessel functions of the 1st and 2nd kind, respectively.

B. Eigenmode Expansion

Next, fields in each region are expressed as a summation of their eigenmodes. Transverse-electromagnetic (TEM^z) and transverse-magnetic (TM^z) fields are considered in Region I and II of the launcher shown in Fig. 1. TEM^z wavenumbers are referred to as $k_i = \omega\sqrt{\mu_0\varepsilon_i}$, where i denotes the region. The TM^z wavenumbers are referred to as k_{zn_i} and $k_{\rho n_i}$ for a discrete n^{th} mode in region i, and are connected by the separation relation: $k_i^2 = k_{zn_i}^2 + k_{\rho n_i}^2$, where k_i is the wavenumber in region i. All regions are air filled, so $k_i = k_0$, and all wavenumbers are in units of radians/meter. The electromagnetic fields are summarized in Table I.

Region I describes the coaxial cable feed. The transverse electromagnetic fields in this region are characterized by an input and reflected TEM^z mode, and a summation of reflected TM^z modes. They are defined by (6) and (7). The forward propagating (incident) TEM^z wave is known, and is assigned magnitude 1 for convenience. Region II describes the leaky radial waveguide or Bessel beam launcher. The transverse electromagnetic fields in this region are a forward and backward propagating (+/-) TEM^z mode and summation of (+/-) TM^z modes, as defined by (8) and (9).

Region III encompasses the free-space beyond the radial waveguide, and is defined for $z > 0$ and $0 \leq \rho < \infty$.

TABLE I. Electromagnetic field profiles for all regions in the single launcher shown in Fig. 1.

Region I	$E_\rho^I(\rho,z) =$	$\left[e^{-jk_1(z+h)} + A_0 e^{jk_1(z+h)}\right]\mathbf{e}^{\mathbf{I}}_{\mathbf{TEM}} + \sum\limits_{n_1=1}^{\infty}\left[-B_{n_1}e^{jk_{zn_1}(z+h)}\right]\mathbf{e}^{\mathbf{I}}_{\mathbf{TM}}$	(6)
	$H_\phi^I(\rho,z) =$	$\left[e^{-jk_1(z+h)} - A_0 e^{jk_1(z+h)}\right]\mathbf{h}^{\mathbf{I}}_{\mathbf{TEM}} + \sum\limits_{n_1=1}^{\infty} B_{n_1}e^{jk_{zn_1}(z+h)}\mathbf{h}^{\mathbf{I}}_{\mathbf{TM}}$	(7)
Region II	$E_\rho^{II}(\rho,z) =$	$\left(C_0e^{-jk_2z} + D_0e^{jk_2z}\right)\mathbf{e}^{\mathbf{II}}_{\mathbf{TEM}} + \sum\limits_{n_2=1}^{\infty}\left(E_{n_2}e^{-jk_{zn_2}z} - F_{n_2}e^{jk_{zn_2}z}\right)\mathbf{e}^{\mathbf{II}}_{\mathbf{TM}}$	(8)
	$H_\phi^{II}(\rho,z) =$	$\left(C_0e^{-jk_2z} - D_0e^{jk_2z}\right)\mathbf{h}^{\mathbf{II}}_{\mathbf{TEM}} + \sum\limits_{n_2=1}^{\infty}\left(E_{n_2}e^{-jk_{zn_2}z} + F_{n_2}e^{jk_{zn_2}z}\right)\mathbf{h}^{\mathbf{II}}_{\mathbf{TM}}$	(9)
Region III	$E_\rho^{III}(\rho,z) =$	$\int\limits_0^\infty Q(k_{\rho_3})\, e^{-jk_{z_3}z}\mathbf{e}^{\mathbf{III}}_{\mathbf{TM}}\partial k_{\rho_3}$	(10)
	$H_\phi^{III}(\rho,z) =$	$\int\limits_0^\infty Q(k_{\rho_3})\, e^{-jk_{z_3}z}\mathbf{h}^{\mathbf{III}}_{\mathbf{TM}}\partial k_{\rho_3}$	(11)

In free-space, the field is expressed as the inverse Hankel transform of the spectrum. The transverse fields in this region are defined in (10) and (11). Note that the free-space spectrum is continuous, rather than discrete, as was the case of the other two regions. Thus, the wavenumbers are expressed as k_{ρ_3} and k_{z_3}, and related by $k_0^2 = k_{z_3}^2 + k_{\rho_3}^2$. The transverse field profiles for the electromagnetic fields defined in Table I are provided in Table II.

C. Boundary Conditions and Power Orthogonality

Next, boundary conditions are enforced on the tangential E_ρ and H_ϕ field components at the interfaces between regions. Following the application of boundary conditions, power orthogonality is applied to simplify expressions. For two eigenmodes, $\bar{\mathrm{e}}_n$ and $\bar{\mathrm{h}}_m$, in the same region, power orthogonality states that:

$$\iint_{\bar{S}} \left[\bar{\mathrm{e}}_n \times \bar{\mathrm{h}}_m^*\right]\cdot\hat{z}\,\partial\bar{S} = 0, \tag{12}$$

when $n \neq m$. $\bar{S}$ defines the cross section of an interface [8, 9, 19–21]. Power orthogonality is applied over the cross-section of the discontinuity to simplify expressions. For brevity, these lengthy derivations are not included in the main text, but can be found in the supplementary material [22].

D. Solution

By exploiting power orthogonality, a system of equations with unknown modal coefficients A_0, B_{n_1}, C_0, D_0, E_{n_2}, and F_{n_2} was written. The free-space spectral coefficient $Q(k_{\rho_3})$ from (10) and (11) was solved in a closed form, and substituted into the system of equations. These detailed calculations are provided in the supplementary material [22]. The system of equations were arranged in a square matrix, $\bar{\bar{M}}$. The mode coefficient vector A and forcing function (excitation) vector W have the relation:

$$\bar{\bar{M}}A = W. \tag{13}$$

The modal coefficient vector can be solved by matrix inversion: $A = \bar{\bar{M}}^{-1}W$. Knowledge of the system dimensions and operating frequency allows all modal coefficients to be solved.

E. Numerical Analysis

In order to test the preceding analysis, the geometrical and electrical parameters for the radial waveguides displayed in Table III were selected. Within Region I, the transverse wavenumbers ($k_{\rho n_1}$) are solved by setting $\mathrm{R}_0(k_{\rho n_1}a, b) = 0$,

$$0 = J_0(k_{\rho n_1}a)\,Y_0(k_{\rho n_1}b) - J_0(k_{\rho n_1}b)\,Y_0(k_{\rho n_1}a)\,. \tag{14}$$

The variable $n_1 = 1, 2, 3\ldots$ defines the higher order TM^z modes in Region 1. To find the cut-off wavenumbers in Region II, $k_{\rho n_1}$ was replaced with $k_{\rho n_2}$, and b with c. For the dimensions given in Table III, the associated TM^z cutoff wavenumbers are given in Table IV.

The operating frequency was chosen to be 10 GHz. The free-space wavenumber at 10 GHz is $k_0 = \omega\sqrt{\mu_0\varepsilon_0} = 209.58$. Due to the small dimensions of Region I, only highly evanescent TM^z modes are present around the design frequency. In other words, the modes are in cutoff. As a result, the TM^z modal coefficients in Region I are many orders of magnitude less than the TEM^z. Since TM^z contributions in Region I are negligible, only the $n_1 = 1$ mode was used in the calculations, whereas $n_2 = 20$ modes were required in Region II for convergence.

F. Results

In this section, numerical results and a discussion of the Bessel launcher are presented. The modal coefficient matrix $\bar{\bar{M}}$ and excitation vector W were computed across the X-band: 8 - 12 GHz. The modal coefficient vector (A) at each frequency were solved for using (13).

TABLE II. Transverse field profiles for all regions in the single launcher shown in Fig. 1, and the coupled launchers in Fig. 5.

	Region I	Region II	Region III	Region IV	Region V
$\mathbf{e_{TEM}}$	$\frac{1}{\rho}$	$\frac{1}{\rho}$	n/a	$\frac{1}{\rho}$	$\frac{1}{\rho}$
$\mathbf{h_{TEM}}$	$\frac{1}{\rho}\sqrt{\frac{\varepsilon_1}{\mu}}$	$\frac{1}{\rho}\sqrt{\frac{\varepsilon_2}{\mu}}$	n/a	$\frac{1}{\rho}\sqrt{\frac{\varepsilon_4}{\mu}}$	$\frac{1}{\rho}\sqrt{\frac{\varepsilon_5}{\mu}}$
$\mathbf{e_{TM}}$	$\frac{k_{\rho n_1}k_{zn_1}}{\omega\varepsilon_1}\mathrm{R}_1\left(k_{\rho n_1}\rho, b\right)$	$\frac{k_{\rho n_2}k_{zn_2}}{\omega\varepsilon_2}\mathrm{R}_1\left(k_{\rho n_2}\rho, c\right)$	$\frac{k_{\rho_3}k_{z_3}}{\omega\varepsilon_3}J_1\left(k_{\rho_3}\rho\right)$	$\frac{k_{\rho n_4}k_{zn_4}}{\omega\varepsilon_4}\mathrm{R}_1\left(k_{\rho n_4}\rho, c\right)$	$\frac{k_{\rho n_5}k_{zn_5}}{\omega\varepsilon_5}\mathrm{R}_1\left(k_{\rho n_5}\rho, b\right)$
$\mathbf{h_{TM}}$	$k_{\rho n_1}\mathrm{R}_1\left(k_{\rho n_1}\rho, b\right)$	$k_{\rho n_2}\mathrm{R}_1\left(k_{\rho n_2}\rho, c\right)$	$k_{\rho_3}J_1\left(k_{\rho_3}\rho\right)$	$k_{\rho n_4}\mathrm{R}_1\left(k_{\rho n_4}\rho, c\right)$	$k_{\rho n_5}\mathrm{R}_1\left(k_{\rho n_5}\rho, b\right)$

1. Input Impedance and Resonance

The single Bessel beam launcher is a 1-port system. The port is a lossless coaxial port at $z = -h$: the boundary between Regions I and II. From (6), the reflection coefficient at this port can be defined as:

$$\Gamma_{in}(z = -h) = \frac{E_\rho^{I-}}{E_\rho^{I+}} \approx A_0, \tag{15}$$

where the $+$ and $-$ superscripts denote forward and backward propagating fields, respectively. Since TM^z modes in Region I are negligible, $\Gamma_{in} \approx A_0$.

Then, the input impedance was calculated to identify the frequencies at which the Bessel launcher resonates. The input impedance is $Z_{in} = Z_0\left(1 + \Gamma_{in}\right)/\left(1 - \Gamma_{in}\right)$, where Γ_{in} is defined by (15), and Z_0 is the characteristic impedance of the coaxial port. Since higher order TM^z modes are considered negligible in Region I, Z_0 is the characteristic impedance of the TEM^z mode in Region I:

$$Z_0 = \sqrt{\frac{\mu}{\varepsilon}}\,\frac{\ln b/a}{2\pi}. \tag{16}$$

Note that $Z_0 = 45.73\ \Omega$ for the conductor dimensions given for Region I in Table III. The resulting $Z_{in} = R_{in} + jX_{in}$ (assuming Z_0 terminations) is complex, and is plotted in Fig. 2. The points of resonance of the structure are identified by the points where $\Re e\left(Z_{in}\right)$ attains a local maximum.

The mode-matching approach was verified using the commercial FEM solver COMSOL Multiphysics. The radial waveguide (with properties in Table III) was embedded in a PEC ground plane. The coaxial port was excited and the frequency domain reflection coefficient extracted. The input impedance was calculated and is plotted in Fig. 2 alongside the results from the mode-matching approach. From the plots in Fig. 2, the predicted resonances agree with the FEM solver to within 0.1%.

TABLE III. Properties of the system depicted in Fig. 1.

Dimension	Value	Descriptor
a	0.653 mm	Inner radius of Region I and II
b	1.4 mm	Outer radius, Region I
c	85.95 mm	Outer radius, Region II
h	1 mm	Radial waveguide height
X_s	-25j Ω	Sheet reactance at 10 GHz

2. The Discrete Waveguide Spectrum

Next, the discrete modes within the waveguide are analyzed to determine points at which a given mode is dominant. The $\hat{z}$-directed TM^z modal strength in the waveguide is the sum of the (+/-) TM^z coefficients: $E_{n_2} + F_{n_2}$. Since the Bessel launcher is electrically thin, the total $\hat{z}$-directed electric field $E_{n_2} + F_{n_2}$ is essentially constant for $-h < z < 0$. The first seven modes of the Bessel beam launcher ($n_2 = 1, 2, \ldots, 7$) are plotted versus frequency in Fig. 3 as $|E_{n_2} + F_{n_2}|$. A direct comparison between Fig. 2 and Fig. 3 shows a correlation between peaks of Z_{in} (resonances) and dominance of a single mode in the waveguide. The frequencies corresponding to peak values of $\Re e(Z_{in})$ and corresponding modal coefficient are recorded in Table V. The frequencies of peak values occur within approximately 1% of each other.

3. Free-Space Fields

An important factor to consider in this leaky waveguide design is the non-diffractive range, d_{diff}, associated with each waveguide mode [1, 6]. The non-diffractive

TABLE IV. TM^z Modes in Region I and II and associated cut-off wavenumbers and frequencies for the system depicted in Fig. 1 with dimensions in Table III.

	Region I		Region II	
Mode (n)	$k_{\rho n_1}$ (rad/m)	f_{n_1} (GHz)	$k_{\rho n_2}$ (rad/m)	f_{n_2} (GHz)
1	4,175.7	199.24	32.3	1.54
2	8,395.4	400.58	69.5	3.32
3			106.7	5.09
4			143.76	6.86
5			180.81	8.63
6			217.82	10.39
7			254.81	12.16

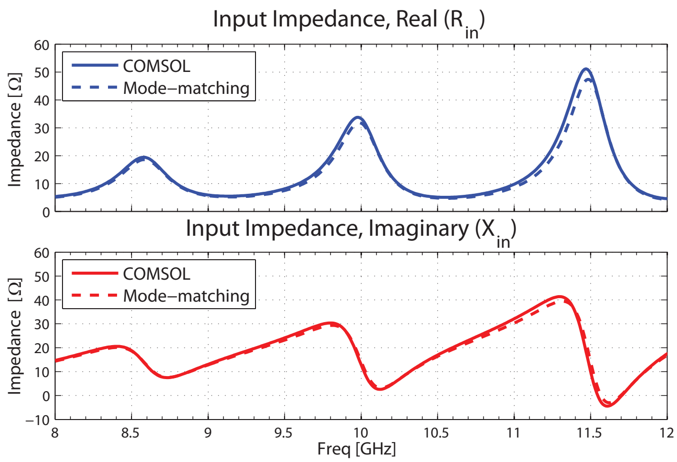

FIG. 2. Real and imaginary input impedance for the single Bessel launcher vs. frequency.

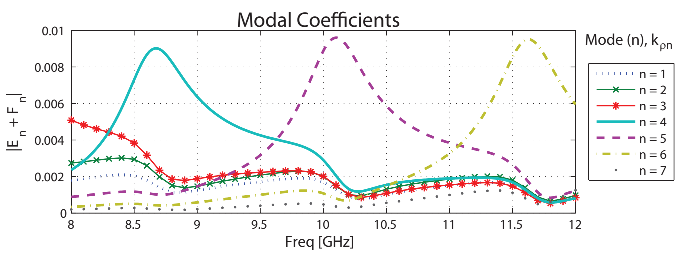

FIG. 3. Magnitudes of the first seven modal coefficients vs. frequency. The coefficients describe the relative strength of each mode in the Bessel Launcher.

range is given by

$$d_{\text{diff}} = c\sqrt{\left(\frac{k_2}{k_{\rho n_2}}\right)^2 - 1}, \tag{17}$$

where k_2 is the wavenumber in the waveguide. Since the launchers are air-filled, $k_2 = k_0$. The values of d_{diff} at a mode's resonant frequency are listed in Table V.

To analyze the fields in free-space, the spectral coefficient, $Q(k_{\rho_3})$, is computed at the resonant frequencies. The $\hat{z}$-directed free-space fields (E_z^{III}) are computed us-

TABLE V. A comparison of point of resonance of Z_{in}, and point at which a given mode experiences its peak strength in the waveguide (Region II). In addition, the non-diffracting region distance (d_{diff}) is displayed for each resonant frequency.

Mode number (n_2)	Wave-number (rad/m)	Resonant frequency (GHz)	Modal peak (GHz)	Percent difference (%)	d_{diff} at resonance (mm)
4	143.76	8.58	8.67	1.05%	64.59
5	180.8	9.99	10.1	1.1%	50.19
6	217.82	11.48	11.63	1.31%	40.32

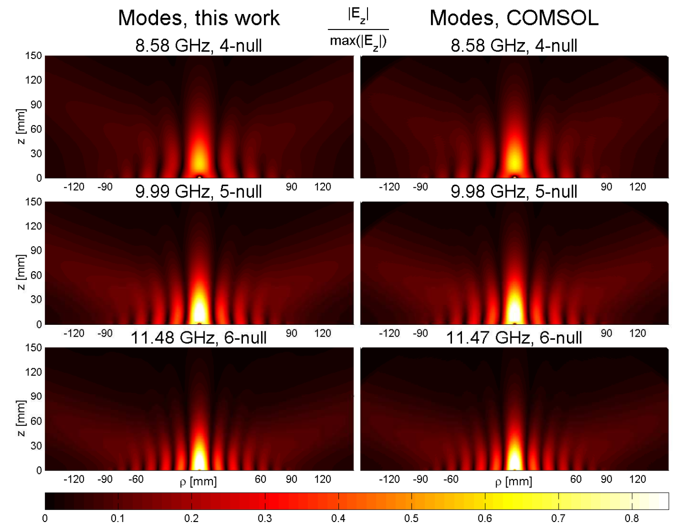

FIG. 4. Normalized electric field $|E_z|/\max(|E_z|)$ in free-space plotted at three resonant frequencies. The left column displays fields plotted using (18). The right column displays the field plots using a commercial FEM solver, COMSOL Multiphysics. The first, second, and third row display the 4, 5, and 6-null Bessel patterns, respectively, at their resonant frequencies. The coordinate system in these plots is the same as that used in Fig. 1. The surface of the launcher extends from $\rho < c$ at $z = 0$ (the bottom axis of each plot). Field patterns have been reflected across $\rho = 0$ to show the complete image.

ing

$$E_z^{III}(\rho, z) = -\frac{j}{\omega\varepsilon_3}\int_0^\infty Q(k_{\rho 3})\, e^{-jk_{z_3}z} J_0(k_{\rho 3}\rho)\, k_{\rho 3}^2 \partial k_{\rho 3}. \tag{18}$$

The free-space fields at the three resonant frequencies in Table V are computed over $0 \leq \rho \leq 150$ mm, and $0 < z \leq 150$ mm. The results are compared to the free-space fields calculated using COMSOL in Fig. 4. A comparison of the field plots indicates close agreement between the mode-matching technique presented here and the commercial solver.

G. Discussion

The extracted electrical characteristics of the Bessel beam launcher demonstrate its core operating principles. The launcher itself supports TM^z modes of an over-sized coaxial metallic geometry excited by an electric field. The input impedance (Fig. 2) of the launcher shows that the structure has multiple resonances. A comparison with the TM^z modal coefficients (Fig. 3) shows that these resonances are associated with the dominance of a single mode in the Bessel launcher. Then, as the free-space field plots show (Fig. 4), the Bessel-function mode excited in the launcher radiates into free-space. The free-space Bessel beam is limited to the non-diffractive region.

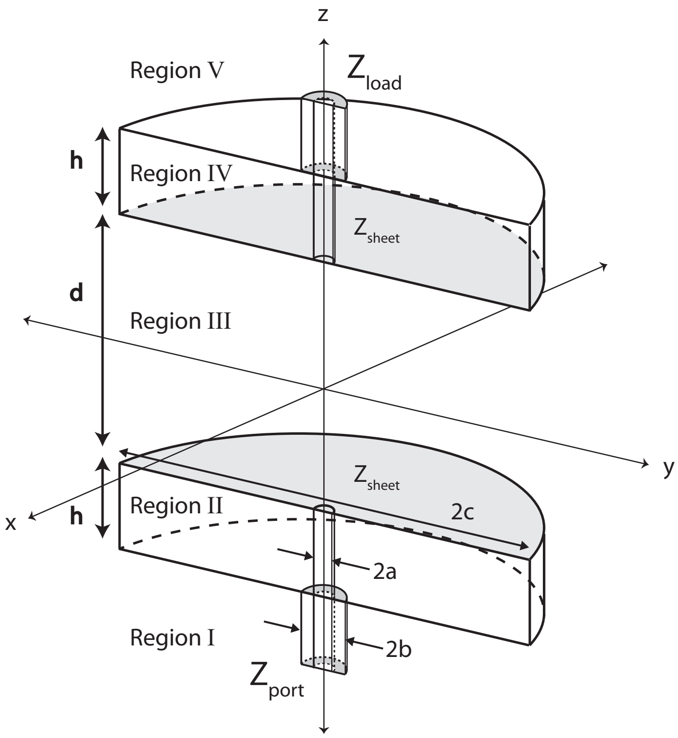

FIG. 5. The cross section of two identical Bessel beam launchers coupled over a distance d. All boundaries, excepting Z_{sheet}, are PEC.

In brief, at a resonance, the Bessel launcher propagates the dominant waveguide mode into free-space.

III. TWO COUPLED BESSEL LAUNCHERS

In this section, the formulation from Section II is extended to consider a system of two coupled Bessel beam launchers, as shown in Fig. 5. The electromagnetic fields within the 5 regions of interest are described next.

A. Definition of Fields

The fields are expressed as a summation of their eigenmodes. Explicit field expressions are summarized in Table VI. Note that the fields are referenced to the center-point between the two launchers. Thus, fields in Regions I, II, and III are rewritten relative to this referencing point. Region I describes the coaxial cable feed, and Region II describes the bottom Bessel beam launcher. Fields in these regions are given by (19)-(22). Region III describes the free-space between the coupled radial waveguides, and is defined for $-\frac{d}{2} < z < \frac{d}{2}$ and $0 \leq \rho < \infty$. In free-space, the transverse fields are given by (23) and (24). Note that the total spectrum consists of forward and backward propagating spectral functions, $Q\left(k_{\rho_3}\right)$ and $P\left(k_{\rho_3}\right)$. These functions are defined at the surface of the bottom and top Bessel beam launcher, respectively.

Region IV describes the top Bessel beam launcher with fields defined by (25) and (26). Region V describes the output coaxial cable. The field expressions in (27) and (28) consider waves incident on and *reflected* from the output coaxial cable (output port). The load reflection coefficient, $\Gamma_L = U_0/T_0$ accounts for TEM^z reflections imposed by the load impedance. It is defined as

$$\Gamma_L = \frac{Z_L - Z_0}{Z_L + Z_0}, \tag{29}$$

where Z_0 is the characteristic impedance of the TEM^z mode (16). Coefficient $\Gamma_L^{TM} = W_{n_5}/S_{n_5}$ accounts for TM^z reflections. As in Region I, the reflections due to TM^z modes are negligible in Region V and are neglected, as the modes are in cutoff. Note that the transverse field profiles for all electromagnetic fields are provided in Table II.

B. Boundary Conditions and Field Solution

Next, the boundary conditions are enforced on E_ρ and H_ϕ at the boundaries between regions. Continuity of power-flow at the boundaries is preserved through power orthogonality operations. The simplification process is lengthy, and is provided in the supplementary material [22].

The coupled Bessel beam launchers are defined by a system of equations with unknown modal coefficients A_0, B_n, C_0, D_0, E_n, F_n, G_0, H_0, K_n, L_n, T_0, S_n, and Γ_L, where Γ_L is a function of the load impedance, and can be arbitrary. These modal coefficients form vector A. In initial calculations, the load is assumed to be matched to the characteristic impedance (Z_0) of the transmission lines of Regions I and V. This is referred to as the port-matched system, as the load is matched to the port impedance. In the port-matched system, $\Gamma_L = 0$. The equations are organized into a matrix $\bar{\bar{M}}$, with a forcing vector W. Then, each coefficient in vector A is solved by matrix inversion (13).

C. A Complex Conjugate Loaded System

An important figure of merit for a coupled system is its transmission efficiency. Efficiency quantifies the amount of energy that is passed from the source to the load. Maximum power transfer is achieved with a simultaneous complex-conjugate impedance-match [23]. In this section, the process to derive the optimal load impedance ($Z_{L,opt}$) that provides a complex-conjugate impedance-match is discussed. Since the structure is symmetric, the optimal source impedance is equal to $Z_{L,opt}$.

The coupled launchers in Fig. 5 form a 2-port system. Port 1 is a lossless coaxial port referenced to the boundary between Regions I and II. Port 2 is similarly

TABLE VI. Electromagnetic field profiles for all regions in the coupled launchers shown in Fig. 5.

Region I	$E_\rho^I(\rho,z) = \left[e^{-jk_1\left(z+\frac{d}{2}+h\right)} + A_0 e^{jk_1\left(z+\frac{d}{2}+h\right)}\right]\mathbf{e}^{\mathbf{I}}_{\mathbf{TEM}} + \sum_{n_1=1}^{\infty}\left[-B_{n_1} e^{jkzn_1\left(z+\frac{d}{2}+h\right)}\right]\mathbf{e}^{\mathbf{I}}_{\mathbf{TM}}$	(19)
	$H_\phi^I(\rho,z) = \left[e^{-jk_1\left(z+\frac{d}{2}+h\right)} - A_0 e^{jk_1\left(z+\frac{d}{2}+h\right)}\right]\mathbf{h}^{\mathbf{I}}_{\mathbf{TEM}} + \sum_{n_1=1}^{\infty} B_{n_1} e^{jkzn_1\left(z+\frac{d}{2}+h\right)}\mathbf{h}^{\mathbf{I}}_{\mathbf{TM}}$	(20)
Region II	$E_\rho^{II}(\rho,z) = \left[C_0 e^{-jk_2\left(z+\frac{d}{2}\right)} + D_0 e^{jk_2\left(z+\frac{d}{2}\right)}\right]\mathbf{e}^{\mathbf{II}}_{\mathbf{TEM}} + \sum_{n_2=1}^{\infty}\left[E_{n_2} e^{-jkzn_2\left(z+\frac{d}{2}\right)} - F_{n_2} e^{jkzn_2\left(z+\frac{d}{2}\right)}\right]\mathbf{e}^{\mathbf{II}}_{\mathbf{TM}}$	(21)
	$H_\phi^{II}(\rho,z) = \left[C_0 e^{-jk_2\left(z+\frac{d}{2}\right)} - D_0 e^{jk_2\left(z+\frac{d}{2}\right)}\right]\mathbf{h}^{\mathbf{II}}_{\mathbf{TEM}} + \sum_{n_2=1}^{\infty}\left[E_{n_2} e^{-jkzn_2\left(z+\frac{d}{2}\right)} + F_{n_2} e^{jkzn_2\left(z+\frac{d}{2}\right)}\right]\mathbf{h}^{\mathbf{II}}_{\mathbf{TM}}$	(22)
Region III	$E_\rho^{III}(\rho,z) = \int_0^{\infty}\left[Q\left(k_{\rho_3}\right) e^{-jkz_3\left(z+\frac{d}{2}\right)} - P\left(k_{\rho_3}\right) e^{jkz_3\left(z-\frac{d}{2}\right)}\right]\mathbf{e}^{\mathbf{III}}_{\mathbf{TM}}\partial k_{\rho_3}$	(23)
	$H_\phi^{III}(\rho,z) = \int_0^{\infty}\left[Q\left(k_{\rho_3}\right) e^{-jkz_3\left(z+\frac{d}{2}\right)} + P\left(k_{\rho_3}\right) e^{jkz_3\left(z-\frac{d}{2}\right)}\right]\mathbf{h}^{\mathbf{III}}_{\mathbf{TM}}\partial k_{\rho_3}$	(24)
Region IV	$E_\rho^{IV}(\rho,z) = \left[G_0 e^{-jk_4\left(z-\frac{d}{2}\right)} + H_0 e^{jk_4\left(z-\frac{d}{2}\right)}\right]\mathbf{e}^{\mathbf{IV}}_{\mathbf{TEM}} + \sum_{n_4=1}^{\infty}\left[K_{n_4} e^{-jkzn_4\left(z-\frac{d}{2}\right)} - L_{n_4} e^{jkzn_4\left(z-\frac{d}{2}\right)}\right]\mathbf{e}^{\mathbf{IV}}_{\mathbf{TM}}$	(25)
	$H_\phi^{IV}(\rho,z) = \left[G_0 e^{-jk_4\left(z-\frac{d}{2}\right)} - H_0 e^{jk_4\left(z-\frac{d}{2}\right)}\right]\mathbf{h}^{\mathbf{IV}}_{\mathbf{TEM}} + \sum_{n_4=1}^{\infty}\left[K_{n_2} e^{-jkzn_4\left(z-\frac{d}{2}\right)} + L_{n_4} e^{jkzn_4\left(z-\frac{d}{2}\right)}\right]\mathbf{h}^{\mathbf{IV}}_{\mathbf{TM}}$	(26)
Region V[a]	$E_\rho^{V}(\rho,z) = \left[T_0 e^{-jk_5\left(z-\frac{d}{2}-h\right)} + U_0 e^{jk_5\left(z-\frac{d}{2}-h\right)}\right]\mathbf{e}^{\mathbf{V}}_{\mathbf{TEM}} + \sum_{n_5=1}^{\infty}\left[S_{n_5} e^{-jkzn_5\left(z-\frac{d}{2}-h\right)} - W_{n_5} e^{-jkzn_5\left(z-\frac{d}{2}-h\right)}\right]\mathbf{e}^{\mathbf{V}}_{\mathbf{TM}}$	
	$= T_0\left[e^{-jk_5\left(z-\frac{d}{2}-h\right)} + \Gamma_L e^{jk_5\left(z-\frac{d}{2}-h\right)}\right]\mathbf{e}^{\mathbf{V}}_{\mathbf{TEM}} + \sum_{n_5=1}^{\infty} S_{n_5}\left[e^{-jkzn_5\left(z-\frac{d}{2}-h\right)} - \Gamma_L^{\mathrm{TM}} e^{-jkzn_5\left(z-\frac{d}{2}-h\right)}\right]\mathbf{e}^{\mathbf{V}}_{\mathbf{TM}}$	(27)
	$H_\phi^{V}(\rho,z) = T_0\left[e^{-jk_5\left(z-\frac{d}{2}-h\right)} - \Gamma_L e^{jk_5\left(z-\frac{d}{2}-h\right)}\right]\mathbf{h}^{\mathbf{V}}_{\mathbf{TEM}} + \sum_{n_5=1}^{\infty} S_{n_5}\left[e^{-jkzn_5\left(z-\frac{d}{2}-h\right)} + \Gamma_L^{\mathrm{TM}} e^{-jkzn_5\left(z-\frac{d}{2}-h\right)}\right]\mathbf{h}^{\mathbf{V}}_{\mathbf{TM}}$	(28)

[a] Coefficient $\Gamma_L = U_0/T_0$ represents TEM^z reflections imposed by the load impedance, and is defined in (29). Coefficient $\Gamma_L^{TM} = W_{n5}/S_{n5}$ accounts for TM^z reflections, and is considered negligible.

defined, and referenced to the boundary between Regions IV and V. In the port-matched case, there are no reflections at Port 2. Such an analysis allows the extraction of the scattering parameters: S_{11}, S_{12}, S_{21}, and S_{21} [24]. Since $A_0 \approx \Gamma_{in} = S_{11}$, an expression for the transmission coefficient ($T = S_{21}$) can be written as

$$T = \frac{E_\rho^{V+}\big|_{d=\frac{d}{2}+h}}{E_\rho^{I+}\big|_{d=-\left(\frac{d}{2}+h\right)}} \approx T_0. \tag{30}$$

As in Region I, contributions from the TM^z modes in Region V are negligible at the frequencies of interest. Thus $T \approx T_0 = S_{21}$. Since the system is symmetric and passive, $S_{22} = S_{11}$ and $S_{12} = S_{21}$.

A simultaneous complex-conjugate impedance-match yields the optimal source and load impedances ($Z_{L,opt}$) [25–27]. If Port 2 is terminated in $Z_{L,opt}$, then this is referred to as the conjugately-matched system, since the load is complex-conjugate impedance-matched. The load also receives maximum power. The derivation of $Z_{L,opt}$ is discussed under such a condition in the Appendix.

D. Numerical Analysis

Now, the process for analyzing the coupled structure with a complex-conjugate load impedance can be clearly defined. For known parameters a, b, c, Z_{sheet}, and h, the procedure involves the following steps:

1. For a given excitation, W, calculate the port-matched $\bar{\bar{M}}$ as a function of frequency ($Z_L = Z_0$, or $\Gamma_L = 0$).
2. Solve for the modal coefficient vector A using (13).
3. Extract $A_0 = S_{11} = S_{22}$, and $T_0 = S_{21} = S_{12}$ from A.
4. Compute Z-parameters from S-parameters [24].
5. Calculate $Z_{L,opt}$ from (A.1) and (A.2).
6. Calculate $\Gamma_{L,opt} = \Gamma_L$ from (29), assuming $Z_L = Z_{L,opt}$.
7. Compute the conjugately-matched $\bar{\bar{M}}'$, using $\Gamma_{L,opt}$ from Step 6. Since the input was not modified, the excitation W is not changed.
8. Solve for the modified coefficient vector A'.

The conjugately-matched system matrix $\bar{\bar{M}}'$ and coefficient vector A' now account for a conjugate impedance-matched load. Modal coefficients for the conjugately-matched system are denoted with a prime notation, and are A_0', B_n', C_0', D_0', E_n', F_n', G_0', H_0', K_n', L_n', T_0', S_n'.

Now that a process for analyzing the structure is defined, the system of coupled launchers was analyzed across the X band: 8 - 12 GHz. In Region II and IV, $n_2 = n_4 = 16$ modes are required for convergence. As before, Regions I and V only consider a single TM^z mode: $n_1 = n_5 = 1$.

E. Results

The 8-step process detailed in the previous section was followed to solve for the modified modal coefficient vector A'. The physical dimensions given in Table III were used in these calculations.

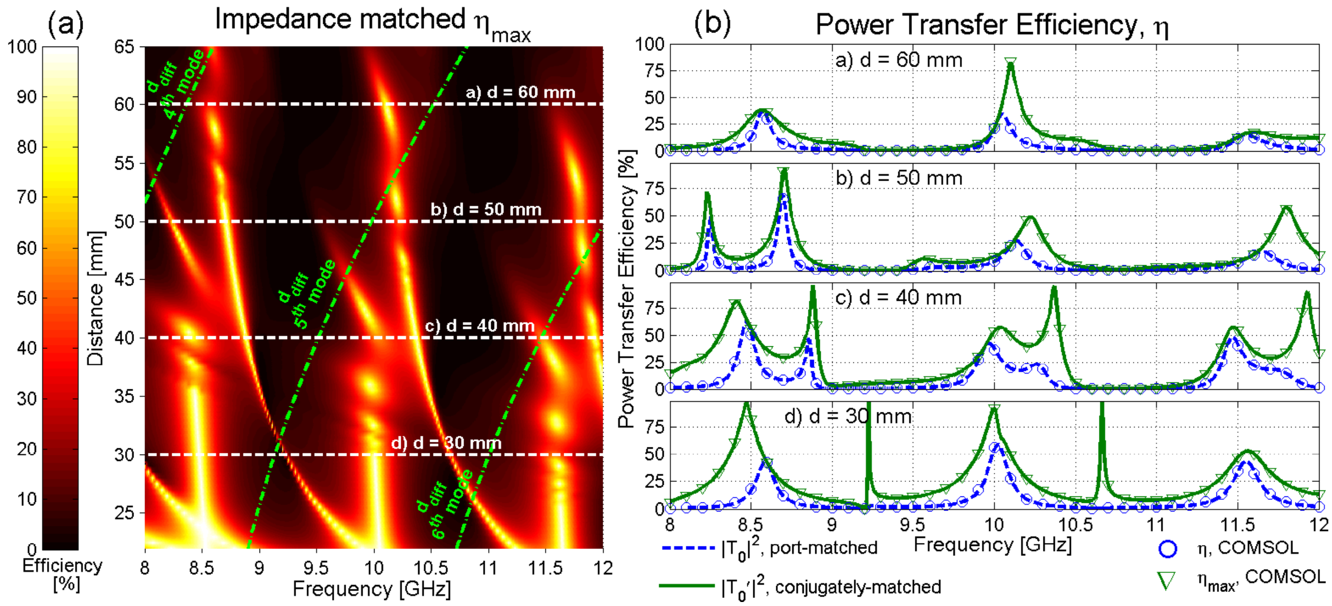

FIG. 6. (a) The conjugately-matched power transfer efficiency ($\eta_{\max}$) calculated from COMSOL using (A.3) is plotted as a colormap, where the height of the colormap is conjugately-matched power transfer efficiency. The non-diffractive range, d_{diff}, of the $n_2 = n_4 = 4, 5$, and 6 mode is included in green dash-dot lines. Four distances of interest have been highlighted ($d =$ 30, 40, 50, and 60, mm). At each distance, a 'slice' of the plot is shown in (b). These slices show the port-matched ($|T_0|^2$ in blue-dashes) and conjugately-matched ($|T_0'|^2$in a green line) power transfer efficiency over frequency calculated using the mode-matching method. Efficiency data from COMSOL, η and $\eta_{\max}$, is overlaid in $\bigcirc$ and ∇, respectively. The plots demonstrate close agreement between the two approaches.

1. Power Transfer

In the port-matched system, $|T_0|^2$ represents the ratio of the power delivered to the load to the power available from the source. This quantity is known as the transducer gain (G_T) of a two port network. Since the port-matched source and load are matched for zero reflections, $G_T = |S_{21}|^2 = |T_0|^2$ [23].

Note that in the conjugately-matched system, the load is modified to present a complex-conjugate match. The source, however, is not modified. Therefore, the power delivered to the input of the network and to the load are defined as

$$P_{IN} = \frac{1}{2Z_0}\left(1 - |A_0'|^2\right), \tag{31}$$

$$P_L = \frac{|T_0'|}{2Z_0}\left(1 - |\Gamma_{L,opt}|^2\right), \tag{32}$$

respectively. The conjugately-matched load reflection coefficient $\Gamma_{L,opt}$ is given by (29) for $Z_L = Z_{L,opt}$. Satisfying the condition for maximum power transfer, $\Gamma_{L,opt} = \Gamma^*_{out}$ (the reflection coefficient looking into port 2). Since the system is symmetric, $\Gamma_{out} = \Gamma_{in} = A_0'$, resulting in $A_0' = \Gamma^*_{L,opt}$ and $|A_0'| = |\Gamma_{L,opt}|$. Finally, the ratio of the power dissipated in the load to the power delivered to the input of the network is

$$G_P = \frac{P_L}{P_{IN}} = |T_0'|\frac{\left(1 - |\Gamma_{L,opt}|^2\right)}{\left(1 - |A_0'|^2\right)} = |T_0'|\,. \tag{33}$$

This quantity is also known as the power gain ($G_P = P_L/P_{IN}$) of a two port network [23, 24]. The power gain is independent of the source impedance. To summarize, the port-matched system efficiency is $|T_0|^2$, while the conjugately-matched system efficiency is $|T_0'|^2$. Note that the conjugately-matched system efficiency is independent of the source impedance.

Next, the system S-parameters were extracted from COMSOL over 8-12 GHz and for d = 0-70 mm. The conjugately-matched power transfer efficiency was calculated over this range using (A.3) and is displayed in Fig. 6a. Using the mode-matching approach (detailed in Section III D), the conjugately-matched modal coefficient vector A' was computed. From it, $|T_0'|^2$ was extracted and is plotted against frequency for 4 separate distances in Fig. 6b. This data is contrasted with $|T_0|^2$ (the *port*-matched case). The results from COMSOL are also overlaid for comparison. The efficiency calculated using the mode-matching approach agrees closely with that computed using COMSOL.

The plots show definite peaks of high power transfer efficiency within the non-diffractive range (d_{diff}) of each Bessel mode. It is also clear that a complex-conjugate

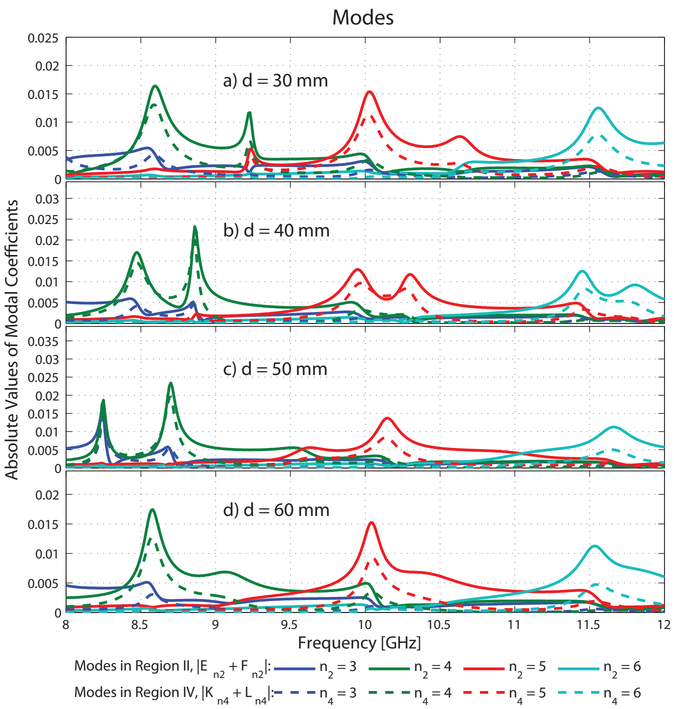

FIG. 7. Modal coefficients in two coupled Bessel beam launchers at $d =$ (a) 30 mm, (b) 40 mm, (c) 50 mm, and (d) 60 mm.

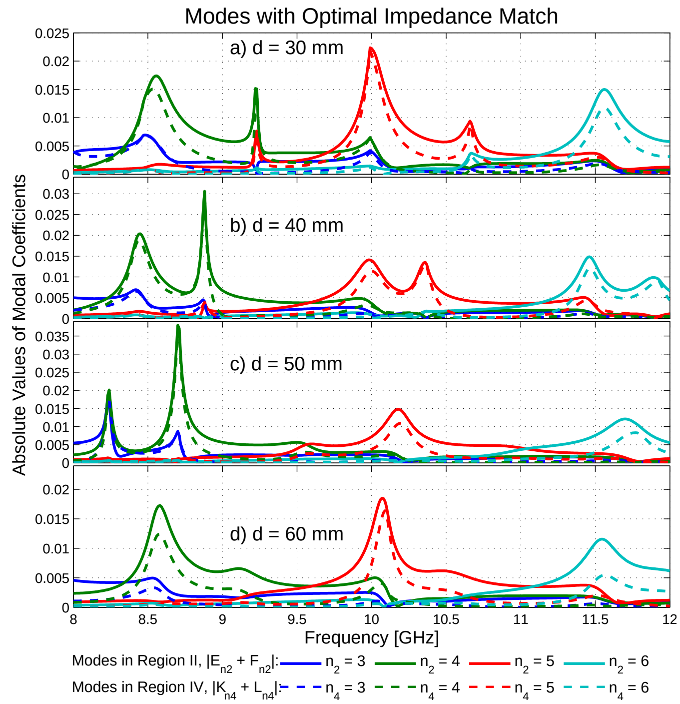

FIG. 8. Modal coefficients in two coupled Bessel beam launchers at $d =$ (a) 30 mm, (b) 40 mm, (c) 50 mm, and (d) 60 mm. A conjugately-matched system is assumed.

impedance-match increases power transfer performance. Next, these traits are further explored in terms of the discrete modes of the coupled launchers.

2. Discrete Waveguide Spectrum

The coefficients (E_{n_2}, F_{n_2}) describe (+/-) TM^z modes in Region II (first launcher), while coefficients (K_{n_4}, L_{n_4}) describe (+/-) TM^z modes in Region IV (second launcher). Since the Bessel launchers are electrically thin, the sum of the coefficients represents the $\hat{z}$-directed total electric field strength in each waveguide over the entire height, h. The quantities $|E_{n_2} + F_{n_2}|$ and $|K_{n_4} + L_{n_4}|$ are plotted versus frequency in Fig. 7 at 4 distances of interest.

3. Analysis of a Conjugately-Matched System

Vector A' provides the conjugately-matched modal coefficients: E'_{n_2},F'_{n_2},K'_{n_4}, and L'_{n_4}. These modified coefficients are displayed as $\left|E'_{n_2} + F'_{n_2}\right|$ and $\left|K'_{n_4} + L'_{n_4}\right|$ in Fig. 8. These values can be directly compared with Fig. 7, the port-matched system.

Firstly, within the non-diffracting range of each Bessel beam, d_{diff} (see Fig 6), the corresponding mode in the launcher is dominant. Additionally, many modes have two maxima; an indication that the modes have split. Mode splitting is a well-known property of coupled resonators, seen, for example, in near-field magnetic resonant power transfer [16]. In order to distinguish the odd and even modes, the phase of the ratio of the dominant modal coefficients in the launchers is calculated:

$$\varphi = \frac{E_{n_2} + F_{n_2}}{K_{n_4} + L_{n_4}}, \tag{34}$$

$$\text{Relative Phase} = \tan^{-1}\left[\frac{\Im m\,(\varphi)}{\Re e\,(\varphi)}\right]. \tag{35}$$

This relative phase determines whether a given peak represents an even or odd mode. When the relative phase $\approx 0^o$, the free-space electric field (E_z^{III}) is even about the xy-plane. Conversely, when the relative phase $\approx 180^o$, E_z^{III} is odd about the xy-plane. This is shown graphically in Fig. 9 a, b. The polarity of each mode's peak at $d = 30$, 40, 50, and 60 mm is displayed in Table VII.

Another interesting facet arises in the conjugately-matched system. The peak modal-strength in the *receiving* waveguide experiences an increase in magnitude over the port-matched system. In other words, at resonance, a complex-conjugate impedance-match significantly strengthens the fields received by the secondary launcher. Additionally, the frequencies of modal-peak-enhancement correspond to frequencies of peak-efficiency. This supports the conclusion that the Bessel launchers are strongly coupled in the radiative near-field. Furthermore, energy is transferred through free-space by the Bessel modes supported by each launcher.

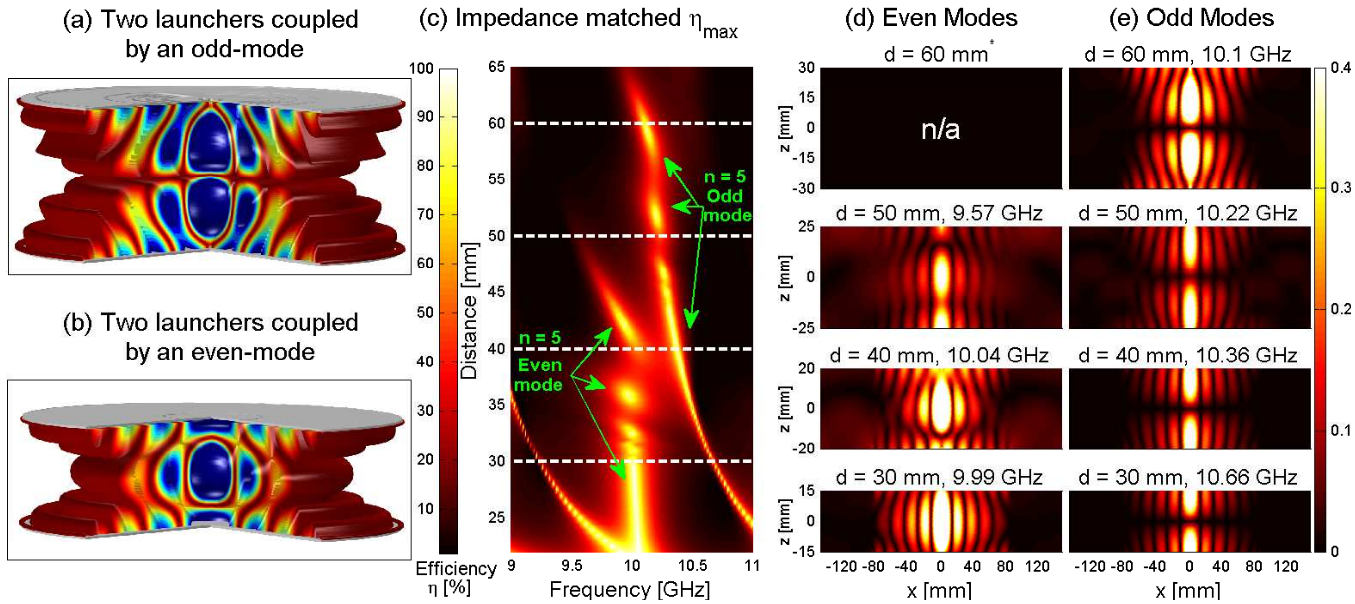

FIG. 9. On the left, in (a) and (b), are renderings of two coupled Bessel launchers experiencing an (a) odd and (b) even mode. In (c), the range of Fig. 6 from 9-11 GHz is displayed (the fifth Bessel mode). The green arrows highlight the efficiency maxima representing the even and odd modes. Plots (d)-(e) demonstrate the even and odd mode free-space E_z^{III} characteristics at power transfer efficiency local maxima. The field plots are normalized: $|E_z/\max(E_z)|$, and the colorbar shows the normalized field value. (*) There is no discernible 5^{th} even-mode at $d = 60$ mm. Here, the even mode has degraded to a point that it does not efficiently transfer power.

TABLE VII. Relative phase of modal coefficients (35) for local maxima in power transfer efficiency.

Port-Matched System ($Z_L = Z_0$)				Conjugately-Matched System ($Z_L = Z_{L,opt}$)			
Mode (n)	f (GHz)	Phase (degrees)	Even/ Odd	Mode (n)	f (GHz)	Phase (degrees)	Even/ Odd
$d = 30$ mm							
4	8.6	-4.8^o	E	4	8.47	-0.2^o	E
4	9.23	193^o	O	4	9.23	191.9^o	O
5	10.02	-5.2^o	E	5	9.99	-0.6^o	E
5	10.64	171.1^o	O	5	10.66	180.5^o	O
6	11.56	0.25^o	E	6	11.56	-0.7^o	E
$d = 40$ mm							
4	8.47	1.63^o	E	4	8.41	0.17^o	E
4	8.86	164.4^o	O	4	8.88	178.2^o	O
5	9.96	15.5^o	E	5	10.04	13.85^o	E
5	10.27	146.4^o	O	5	10.37	178.5^o	O
6	11.46	17.87^o	E	6	11.47	10.61^o	E
6	-	-	O	6	11.93	178^o	O
$d = 50$ mm							
4	8.25	4.01^o	E	4	8.23	2.34^o	E
4	8.69	170.9^o	O	4	8.71	179.2^o	O
5	10.15	173.9^o	O	5	10.22	176.7^o	O
6	11.65	170.4^o	O	6	11.8	181.8^o	O
$d = 60$ mm							
4	8.57	177^o	O	4	8.56	177.1^o	O
5	10.05	190.7^o	O	5	10.1	181.9^o	O
6	11.54	197.4^o	O	6	11.59	202.6^o	O

4. Free Space Fields

Next, the characteristics of the free-space fields at a mode are discussed. The free-space fields are plotted for frequencies corresponding to the peaks of $|T_0'|^2$ in Fig. 6. At these frequencies, the most power is transferred. E_z in Region III is given by

$$E_z^{III}(\rho, z) = -\frac{j}{\omega\varepsilon_3}\int_0^\infty \Big[Q(k_{\rho 3})\, e^{-jk_{z_3}\left(z+\frac{d}{2}\right)} + P(k_{\rho 3})\, e^{jk_{z_3}\left(z-\frac{d}{2}\right)}\Big] J_0(k_{\rho 3}\rho)\, k_{\rho 3}^2 \partial k_{\rho 3}. \quad (36)$$

The even and odd $n_2 = n_4 = 5$ free-space fields are plotted in Fig. 9 d, e, for a conjugately-matched system. Note that as distance increases, the even mode field becomes more diffuse, whereas a sharp field pattern persists for the odd-mode. Additionally, the odd-mode fields are tightly constrained to the region between the two launchers ($\rho < c$). Since the structures are lossless, it is clear from Fig. 6 that the even modes radiate significantly more power into free-space. This indicates that the odd mode is a preferred choice for high-Q coupling. In fact, the fields of an odd-mode appear as those in a waveguide, but occur in free-space.

F. Discussion

The coupling performance of two Bessel launchers was reported. The two launchers demonstrate characteristics of strongly coupled resonators. The modes of a launcher in isolation are split into even and odd modes in the coupled system (Fig. 8). By modifying the analysis to consider a conjugately-matched system, the receiving launcher's field amplitudes were enhanced, resulting in an increased efficiency (Fig. 6). Though it was shown that both even and odd modes can transfer power, odd modes are preferred due to the stronger field confinement and the resulting higher efficiency.

At close distances ($d < d_{\text{diff}}$), the even and odd $n_2 = n_4 = 5$ modes demonstrate marked free-space field enhancement (see Fig. 9). However, the degradation of the even mode becomes more apparent as d increases. When $d = 60$ mm, the even mode fields become more diffuse as the majority of power is radiated. What is curious is that even for $d > d_{\text{diff}}$, the $n = 5$ odd mode persists for some distance.

Also of note, despite being a radiative system, the transmitting and receiving Bessel launchers are highly coupled. Several electrical parameters of the transmitting radiator depend on the receiving radiator. As the receiver is perturbed, the input impedance of the transmitter changes, as well as optimal load impedance. In far-field wireless systems this is not the case since the coupling coefficient between transmitting and receiving radiators is low.

The radiation properties behind the even and odd modes can be explained in terms of equivalent magnetic currents. The $+\hat{z}$ electric field near the lower launcher can be represented by a $+\hat{\phi}$-directed magnetic current. In an odd mode, the $-\hat{z}$ fields near the upper launcher are represented by a $-\hat{\phi}$ magnetic current. In the far-field, these opposing sources destructively interfere, reducing radiation losses. However, for an even mode, the electric field maintains a $+\hat{z}$ direction between the launchers, reinforcing the $+\hat{\phi}$-directed magnetic current and radiating energy into free-space. This explains why the odd mode provides higher field confinement and power transfer efficiency.

IV. CONCLUSION

In this work, a planar Bessel beam launcher at microwave frequencies was analyzed through Eigenmode expansion and mode matching analysis. Boundary conditions were enforced on tangential field components and simplified by power orthogonality relations. The numerical solution provides a modal breakdown of a coaxial-fed Bessel beam launcher. It allows the input impedance and discrete waveguide-modes to be plotted over frequency. At the frequencies of resonance, the free-space fields were plotted using the Hankel transform. The analysis showed that a Bessel beam launcher operating at a resonant frequency has one dominant waveguide mode that propagates into free-space.

Further, the work was extended to analyze a wireless link employing Bessel beams. A simultaneous complex conjugate impedance-match was applied to two coupled launchers. Waveguide mode coefficients were plotted for each launcher, and the even and odd modes of the coupled system were identified. Results show that the conjugately-matched system experiences higher transmission efficiency at the even or odd modes. Also, free-space field plots showed that the conjugately-matched system has a high degree of field confinement. In fact, the field distribution appears as that within a waveguide, despite operating in free-space. However, as the coupling distance increases, the even modes are no longer sustainable and radiate into free-space. In contrast, the conjugately-matched odd modes have a comparatively high degree of field containment. As a result, the odd modes couple more efficiently as distance increases between two coupled Bessel launchers.

Single Bessel beam launchers have several potential applications. The structure used in this work can be modified to produce collimated Bessel beams [28]. Using a layered metasurface, launchers have been used to develop low-profile high-gain antennas [29]. Using a similar approach, tractor beams [30] have been realized for microparticle manipulation. Further, vector Bessel beams, such as those reported here, have been shown to be self-healing [31]. This can result in robust systems whose main beam remains unperturbed outside the shadow region of obstacles. Coupled Bessel beam launchers also have several potential applications. The high degree of field confinement and coupling indicates applications in power transfer and covert communication. Additionally, free-space high Q resonators could be used in nondestructive evaluation [32] to simplify material parameter extraction [33].

ACKNOWLEDGMENTS

This work was supported by a National Defense Science and Engineering Graduate Fellowship, the Air Force Office of Scientific Research (AFOSR) under AFOSR grant FA9550-15-1-0101, and the KACST Center for Microwave Sensor Technology.

Appendix: Deriving $Z_{L,opt}$ from S-parameters

The reflected and incident waves of a 2-port system (such as two coupled Bessel launchers as described in Section III) are characterized by a 2×2 S-parameter matrix. From this S-parameter matrix, the Z-parameters can be computed [24]. A simultaneous complex-conjugate impedance-match yields the following expressions for the optimal source and load impedances [25–27]:

$$\Re e\left[Z_L\right]=\sqrt{\Re e^2\left[Z_{22}\right]-\frac{\Im m^2\left[{Z_{12}}^2\right]}{4\Re e^2\left[Z_{11}\right]}-\frac{\Re e\left[Z_{22}\right]}{\Re e\left[Z_{11}\right]}\Re e\left[{Z_{12}}^2\right]}, \tag{A.1}$$

$$\Im m\left[Z_L\right]=\frac{\Im m\left[{Z_{12}}^2\right]}{2\Re e\left[Z_{11}\right]}-\Im m\left[Z_{22}\right], \tag{A.2}$$

where (A.1) and (A.2) are the real and imaginary parts of the optimal port impedance: $Z_{L,opt} = \Re e\left[Z_L\right] + j\Im m\left[Z_L\right]$.

If Port 2 is terminated in $Z_{L,opt}$, then the load also receives maximum power. From (A.1) and (A.2), the conjugately-matched power transfer efficiency can be calculated. It is defined as the ratio of the power delivered to the load (P_L) to the power available from the source (P_{AVS}) [27]:

$$\begin{aligned}\eta_{\max} &= \frac{P_L}{P_{AVS}}\\ &= \frac{\left|Z_{21}\right|^2}{2\Re e\left[Z_{11}\right]\left(\Re e\left[Z_{22}\right]+\Re e\left[Z_{L,opt}\right]\right)-\Re e\left[Z_{21}^2\right]}.\end{aligned} \tag{A.3}$$

[1] J. Durnin, "Exact solutions for nondiffracting beams. I. The scalar theory," J. Opt. Soc. Am. A **4**, 651–654 (1987).

[2] W. B. Williams and J. B. Pendry, "Generating Bessel beams by use of localized modes," Journal of the Optical Society of America A **22**, 992–997 (2005).

[3] R. M. Herman and T. A. Wiggins, "Production and uses of diffractionless beams," Journal of the Optical Society of America A **8**, 932–942 (1991).

[4] S. K. Tiwari, S. R. Mishra, S. P. Ram, and H. S. Rawat, "Generation of a Bessel beam of variable spot size," Applied Optics **51**, 3718–3725 (2012).

[5] G. S. Sokolovskii, V. V. Dudelev, S. N. Losev, M. Butkus, K. K. Soboleva, A. I. Sobolev, A. G. Deryagin, V. I. Kuchinskii, W. Sibbett, and E. U. Rafailov, "Influence of the axicon characteristics and beam propagation parameter M^2 on the formation of Bessel beams from semiconductor lasers," Quantum Electronics **43**, 423–427 (2013).

[6] M. Ettorre and A. Grbic, "Generation of propagating Bessel beams using leaky-wave modes," IEEE Transactions on Antennas and Propagation **60**, 3605–3613 (2012).

[7] M. Ettorre, S. Rudolph, and A. Grbic, "Generation of propagating Bessel beams using leaky-wave modes: experimental validation," IEEE Transactions on Antennas and Propagation **60**, 2645–2653 (2012).

[8] A. Wexler, "Solution of waveguide discontinuities by modal analysis," Microwave Theory and Techniques, IEEE Transactions on **15**, 508–517 (1967).

[9] P. J. B. Clarricoats and K. R. Slinn, "Numerical solution of waveguide-discontinuity problems," Electrical Engineers, Proceedings of the Institution of **114**, 878–886 (1967).

[10] G. V. Eleftheriades, A. S. Omar, L. P. B. Katehi, and G. M. Rebeiz, "Some important properties of waveguide junction generalized scattering matrices in the context of the mode matching technique," Microwave Theory and Techniques, IEEE Transactions on **42**, 1896–1903 (1994).

[11] R. Rodriguez-Berral, F. Mesa, and F. Medina, "Analytical multimodal network approach for 2-D arrays of planar patches/apertures embedded in a layered medium," Antennas and Propagation, IEEE Transactions on **63**, 1969–1984 (2015).

[12] S. Aksimsek, G. Cinar, B. Nilsson, and S. Nordebo, "TEM wave scattering by a step discontinuity on the outer wall of a coaxial waveguide," Microwave Theory and Techniques, IEEE Transactions on **61**, 2783–2791 (2013).

[13] J. H. Kim D. Y. Na, K.-Y. Jung, and Y. B. Park, "Mode-matching analysis of a coaxially fed annular slot surrounded with corrugations," Electromagnetics **34**, 92–110 (2014).

[14] W. C. Brown, "The history of power transmission by radio waves," IEEE Transactions on Microwave Theory and Techniques **32**, 1230–1242 (1984).

[15] A. Kurs, A. Karalis, R. Moffatt, J. D. Joannopoulos, P. Fisher, and M. Soljačić, "Wireless power transfer via strongly coupled magnetic resonances," SCIENCE **317**, 83–86 (2007).

[16] J. D. Heebl, E. M. Thomas, R. P. Penno, and A. Grbic, "Comprehensive analysis and measurement of frequency-tuned and impedance-tuned wireless non-radiative power-transfer systems," Antennas and Propagation Magazine, IEEE **56**, 131–148 (2014).

[17] R. Want, "An introduction to RFID technology," IEEE Pervasive Computing **5**, 25–33 (2006).

[18] C. A. Balanis, *Advanced Engineering Electromagnetics* (John Wiley and Sons, Inc., 1989).

[19] R. Harrington, *Time-Harmonic Electromagnetic Fields* (Wiley-IEEE Press, 2001).

[20] E. B. Manring and Jr. Asmussen, J., "Energy and power orthogonality in isotropic, discretely inhomogeneous waveguides," Microwave and Guided Wave Letters, IEEE **3**, 78–79 (1993).

[21] P. R. McIssac, E. B. Manring, and J. Asmussen, "Comments on 'Energy and power orthogonality in isotropic, discretely inhomogeneous waveguides' (and reply)," Microwave and Guided Wave Letters, IEEE **3**, 284–285 (1993).

[22] See Supplemental Material at [URL will be inserted by publisher] for in-depth derivations of the simplified boundary conditions of a single Bessel beam launcher, and two coupled Bessel beam launchers.

[23] G. Gonzalez, *Microwave Transistor Amplifiers: Analysis and Design*, 2nd ed. (Prentice Hall, Inc., 1997).

[24] D. M. Pozar, *Microwave Engineering*, 2nd ed. (John Wiley and Sons, Inc., 1998).

[25] M. Ettorre, M. Casaletti, and A. Grbic, "Power link budget for propagating Bessel beams," in *Antennas and Propagation Society International Symposium (APSURSI)* (2013) pp. 960–961.

[26] J. Rahola, "Power waves and conjugate matching," IEEE Transactions on Circuits and Systems II: Express Briefs

55, 92–96 (2008).

[27] M. Ettorre and A. Grbic, "A transponder-based, nonradiative wireless power transfer," IEEE Antennas and Wireless Propagation Letters **11**, 1150–1153 (2012).

[28] C. Pfeiffer and A. Grbic, "Controlling vector Bessel beams with metasurfaces," Phys. Rev. Applied **2**, 044012 (2014).

[29] C. Pfeiffer and A. Grbic, "Planar lens-antennas of subwavelength thickness: collimating leaky-waves with metasurfaces," Antennas and Propagation, IEEE Transactions on **63**, 3248–3253 (2015).

[30] C. Pfeiffer and A. Grbic, "Generating stable tractor beams with dielectric metasurfaces," Phys. Rev. B **91**, 115408 (2015).

[31] G. Milione, A. Dudley, T. A. Nguyen, O. Chakraborty, E. Karimi, A. Forbes, and R. R. Alfano, "Measuring the self-healing of the spatially inhomogeneous states of polarization of vector Bessel beams," Journal of Optics **17**, 035617 (2015).

[32] H. G. Akhavan and D. Mirshekar-Syahkal, "Slot resonators for characterization of dielectrics at microwave frequencies," in *Review of Progress in Quantitative Non-Destructive Evaluation (QNDE)*, Vol. 16 (1997).

[33] P. F. Goldsmith, *Quasioptical systems: gaussian beam quasioptical propagation and applications* (Wiley-IEEE Press, 1998).